JGR Atmospheres

RESEARCH ARTICLE
10.1029/2022JD038092

Horizontal Correlation Functions of Wind Fluctuations in the Mesosphere and Lower Thermosphere

Facundo L. Poblet[1], Juha Vierinen[2], Victor Avsarkisov[1], J. Federico Conte[1], Harikrishnan Charuvil Asokan[1], Christoph Jacobi[3], and Jorge L. Chau[1]

[1]Leibniz Institute of Atmospheric Physics at the University of Rostock, Kühlungsborn, Germany, [2]Arctic University of Norway, Tromsø, Norway, [3]Institute for Meteorology, Leipzig University, Leipzig, Germany

Key Points:

- A more efficient estimator for horizontal correlation functions is introduced
- The rotational and divergent correlation functions of mesosphere and lower thermosphere wind fluctuations are found to be balanced at horizontal mesoscales
- Horizontal correlations of wind fluctuations follow a 2/3-power law for horizontal separations of up to 300–400 km

Correspondence to:
F. L. Poblet,
poblet@iap-kborn.de

Citation:
Poblet, F. L., Vierinen, J., Avsarkisov, V., Conte, J. F., Charuvil Asokan, H., Jacobi, C., & Chau, J. L. (2023). Horizontal correlation functions of wind fluctuations in the mesosphere and lower thermosphere. *Journal of Geophysical Research: Atmospheres*, *128*, e2022JD038092. https://doi.org/10.1029/2022JD038092

Received 27 OCT 2022
Accepted 17 FEB 2023

Abstract Measurements of kinetic energy in vortical and divergent fluctuations in the mesosphere and lower thermosphere can be used to study stratified turbulence (ST) and gravity waves. This can be done using horizontal correlation functions of the fluctuating component of velocity. This study introduces a novel method for estimating these correlation functions using radars that observe Doppler shifts of ionized specular meteor trails. The technique solves the correlation functions directly on a longitudinal-transverse-up coordinate system, assuming axial symmetry. This procedure is more efficient and leads to smaller uncertainties than a previous approach. The new technique is applied to a year-long data set from a multistatic specular meteor radar network in Germany, to study the annual variability of kinetic energy within turbulent fluctuations at 87–93 km of altitude. In monthly averages, the kinetic energy is found to be nearly equipartitioned between vortical and divergent modes. Turbulent fluctuations maximize during the winter months with approximately 25% more energy in these months than at other times. The horizontal correlation functions are in agreement with the inertial subrange of ST, exhibiting a 2/3 power law in the horizontal lag direction, with an outermost scale of ST to be about 380 km. This suggests that horizontal correlation functions could be used to estimate turbulent energy transfer rates.

Plain Language Summary Flows exhibit a phenomenon called turbulence, which transfers energy from large scales into smaller scales. This effect is important to quantify the energy budget of the Earth's upper atmosphere. The range of length scales where this phenomenon occurs is called the inertial subrange of turbulence. The classical theory of isotropic turbulence predicts that this energy transfer occurs on length scales smaller than ∼100 m, at 60–110 km altitude. Recent work has shown that horizontal velocity fluctuations can extend the inertial subrange to length scales of up to hundreds of kilometers horizontally. This type of turbulence is called stratified turbulence (ST). So far no comprehensive study has been made to experimentally examine ST in the mesosphere and lower thermosphere (MLT) region on horizontal mesoscales. This study introduces a method for doing so by measuring how the wind fluctuations are correlated as a function of horizontal separation. This is achieved by using meteor radar measurements. The technique is applied to a year-long data set over Germany. It is found that the MLT wind fluctuations are compatible with ST theory. The introduced method could potentially be used for routinely measuring how kinetic energy flows from large-scale to small-scale atmospheric fluctuations.

1. Introduction

The statistical concept of correlation functions is essential for characterizing many aspects of geophysical fluid dynamics. In the context of turbulence theory, they are considered the "workhorse" (Davidson, 2004, p. 88) from which other quantities are defined (Batchelor, 1953; Stull, 1988). They can be used, for instance, to test the validity of stratified turbulence (ST) theory in the middle atmosphere. Lindborg (2006) advanced the concept postulated in previous works (Gage, 1979; Lilly, 1983), that horizontal mesoscales can exhibit an inertial subrange in the context of ST, similar to the inertial subrange of three-dimensional Kolmogorov turbulence, theorized by Richardson (1922) and Kolmogorov (1941). This may account for the −5/3 slope in the horizontal wavenumber spectra of winds, as observed by Nastrom et al. (1984). Many authors have found indications of such a subrange using second-order structure functions (e.g. Cho & Lindborg, 2001; Lindborg, 2007; Rodriguez Imazio et al., 2022) that are algebraically equivalent to correlation functions in a homogeneous medium. They found that structure functions follow a consistent 2/3-power law of separation distance, which is equivalent to a −5/3-power law behavior in the wavenumber domain. Velocity correlation functions can also be employed to perform a

Helmholtz decomposition (Lindborg, 2014). The separation into rotational and divergent modes of motion across a wide range of spatial scales enables establishing dominant physical mechanisms when moving from synoptic scales phenomena to mesoscale and kilometer scale variations (Callies et al., 2016; Hamilton et al., 2008; Skamarock et al., 2014).

Spatial correlations tell us about the manner and degree to which certain parameters (e.g., temperature, velocity, density) are correlated, when measured at different locations. For the neutral atmosphere, comprehensive studies have been performed using second-order structure functions, implemented over different databases made by commercial aircraft measurements. For example, Cho and Lindborg (2001) calculated velocity structure functions using the Measurement of Ozone and Water Vapor by Airbus In-Service Aircraft database (Marenco et al., 1998), for separation ranges with varying resolutions, dividing in four latitude ranges and discriminating between tropospheric and stratospheric measurements. They found that structure functions at a separation distance of ∼100 km increase with latitude in the troposphere and decrease with latitude in the stratosphere. Similarly, Frehlich and Sharman (2010) carried out a comprehensive study of temperature and velocity structure functions using the Aircraft Communications, Addressing, and Reporting System/Aircraft Meteorological Data Relay database, and were able to estimate, among others, the climatology of horizontal structure functions, and to determine eddy dissipation rates from them.

Until recently, studies of spatial correlation functions or structure functions in the atmosphere were mostly limited to the upper troposphere—lower stratosphere (UTLS) region, since measurements of the wind velocity vector for a large enough geographic region are rare and sparse for higher altitudes. A recently introduced technique that uses second-order statistics of line-of-sight drift velocities, measured using meteor radars, has made it possible to estimate spatial and temporal correlation functions of winds in the mesosphere and lower thermosphere (MLT) region. We refer to this technique as Wind Field Correlation Function Inversion (WCFI). One of the results of Vierinen et al. (2019) was that the horizontal structure functions of the horizontal fluctuating wind follow a 2/3-power law for horizontal separations up to about 400 km, consistent with a turbulent cascade of energy into smaller scales.

Poblet et al. (2022) applied the WCFI technique and found the two dimensional horizontal correlation functions of zonal and meridional fluctuating winds to be approximately axisymmetric. This result allowed them to transform the two-dimensional correlations to longitudinal and transverse components. This decomposition can be used to study the balance between the correlations of vertical vorticity and horizontal divergence. Based on a week-long special data set, the study found an imbalance between vertical vorticity and horizontal divergence correlations.

Motivated by the need of estimating correlation functions with smaller uncertainties and on longer data sets, this study introduces a numerically and statistically more efficient technique to estimate horizontal correlation functions of the longitudinal and transverse winds. The new technique is applied to a year-long data set in Germany, to study the annual variability of kinetic energy across various horizontal scales. The resulting correlation functions are also used to study the annual variability of rotational and divergent correlations that can be estimated with the compact expressions given by Lindborg (2014, Eqs. 2.5 and 2.6).

2. Method

When measuring the Doppler shift of a specular meteor trail echo (ω), specular meteor radars (SMRs) observe a one-dimensional projection of the mesospheric wind $(\vec{u})$ on the Bragg wave vector $(\vec{k})$, plus a Doppler shift measurement error (ξ) (e.g., Hocking et al., 2001; Holdsworth et al., 2004):

$$\omega = \vec{k} \cdot \vec{u} + \xi. \tag{1}$$

Vectors $\vec{k}$ and $\vec{u}$ in Equation 1 can be written in different coordinate systems that result in different representations of the vector components. A typical coordinate system used to study the wind dynamics is the east-north-up (ENU) system, in which $\vec{u}$ is decomposed in zonal (u), meridional (v) and vertical (w) components. This decomposition is very useful to study phenomena with recurrent strong directionalities in the atmosphere like planetary waves or tides. The Earth's rotation provides a reference, to which large-scale processes are more sensitive.

On the contrary, to study turbulence using correlation functions or second order structure functions, the longitudinal-transverse-up (LTz) coordinate system is commonly used (e.g., Batchelor, 1953; Buell, 1960; Cho

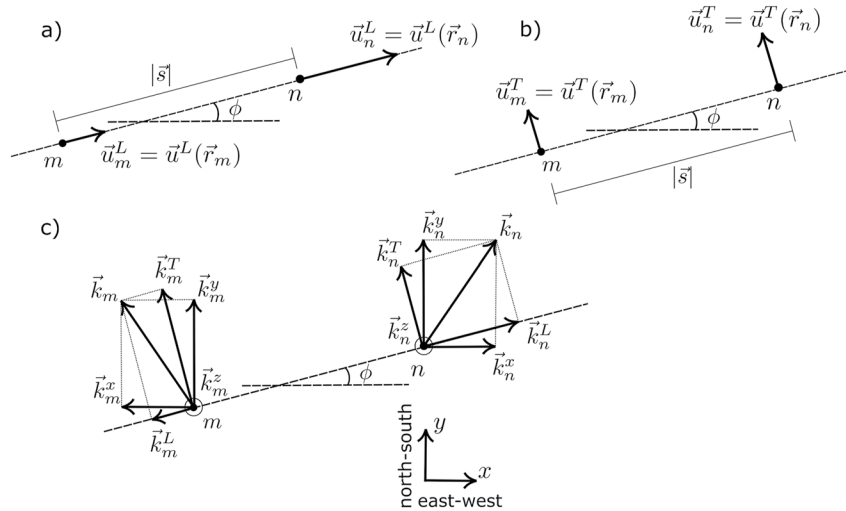

Figure 1. (a) Longitudinal components of the wind velocity $(\vec{u}^L)$ at the positions of meteors n and m. Each pair of meteor detections defines a different longitudinal-transverse-up (LTz) system to decompose the vectors. The angle ϕ is defined between the east-west direction and the longitudinal direction, and $|\vec{s}|$ is the separation distance between the positions of meteors n and m. (b) Same as Panel (a) but for the transverse component of the wind velocity $(\vec{u}^T)$. (c) The vectors $\vec{k}_n$ and $\vec{k}_m$ are the Bragg wave vectors of the meteors n and m. Their decomposition in the LTz system and in east-north-up coordinate system is shown. In terms of the vector components these are $\vec{k}_m = \vec{k}_m^L + \vec{k}_m^T + \vec{k}_m^z = \vec{k}_m^x + \vec{k}_m^y + \vec{k}_m^z$ and $\vec{k}_n = \vec{k}_n^L + \vec{k}_n^T + \vec{k}_n^z = \vec{k}_n^x + \vec{k}_n^y + \vec{k}_n^z$.

& Lindborg, 2001; Frehlich & Sharman, 2010; King et al., 2015a, 2015b; Lindborg, 1999). With this convention, every pair of measurements in space, for example, m, n ($m \neq n$), defines the particular direction from which the components are established. The longitudinal direction is along the line that connects a pair of meteor positions, and the transverse direction is perpendicular to this line.

The velocity in the position and time of the point n, denoted as $\vec{u}_n = \vec{u}(t_n, \vec{r}_n)$, is decomposed in three orthogonal vectors as $\vec{u}_n = \vec{u}_n^L + \vec{u}_n^T + \vec{w}_n$, in which $\vec{w}_n$ is in the local vertical direction, $\vec{u}_n^L$ is perpendicular to $\vec{w}_n$ along the line that connects the position of m and n, and $\vec{u}_n^T$ is perpendicular to $\vec{u}_n^L$ and $\vec{w}_n$. For $\vec{u}_m = \vec{u}(t_m, \vec{r}_m)$, the equivalent decomposition is given by $\vec{u}_m = \vec{u}_m^L + \vec{u}_m^T + \vec{w}_m$. Panels (a) and (b) of Figure 1, adapted from Batchelor (1953, Figure 3.1), illustrate the vector components in the LTz decomposition. The plot in Panel (a) shows the longitudinal components at the points separated by $\vec{s}$, seen from the vertical direction. Similarly, the plot of Panel (b) shows the transverse components. The angle ϕ is the angle from the east-west direction and depends exclusively on the positions of the points n and m.

The LTz decomposition of the Bragg vector at the points n and m is defined as $\vec{k}_n = \vec{k}_n^L + \vec{k}_n^T + \vec{k}_n^z$ and $\vec{k}_m = \vec{k}_m^L + \vec{k}_m^T + \vec{k}_m^z$, respectively. The vectors $\vec{k}_m$ and $\vec{k}_n$ are schematically presented in Figure 1c. In addition to the LTz decomposition, this panel shows the ENU components decomposition, that is, $\vec{k}_m = \vec{k}_m^x + \vec{k}_m^y + \vec{k}_m^z$ and $\vec{k}_n = \vec{k}_n^x + \vec{k}_n^y + \vec{k}_n^z$, in which the superscript x denotes the east-west direction, y denotes the north-south direction, and z represents the up-down direction. The relations between the horizontal components in the two systems, for the point n (similarly for point m) are given by

$$k_n^L = k_n^x \cos\phi + k_n^y \sin\phi, \tag{2}$$

$$k_n^T = -k_n^x \sin\phi + k_n^y \cos\phi. \tag{3}$$

These relations are deduced by considering the well-known conversion of a vector from Cartesian to cylindrical components, or by using geometrical arguments in Figure 1b, and are valid when the points n and m are not separated too much. For large separations, the local vertical directions differ significantly and ϕ loses meaning. Yet, relations 2 and 3 work properly for the horizontal scales investigated in this work (see Section 3). We shall see in Section 2.1 that if the Bragg vectors $\vec{k}$ are represented in LTz components, then the solutions for the correlations of $\vec{u}$ using WCFI are in LTz as well.

2.1. Correlation Function Disambiguation

Consider two different meteors n and m, located at positions $\vec{r}_n$ and $\vec{r}_m$; and occurring at times t_n and t_m. We denote their Doppler shifts as $\omega_n = \omega(t_n, \vec{r}_n)$ and $\omega_m = \omega(t_m, \vec{r}_m)$, measurement errors given by $\xi_n = \xi(t_n, \vec{r}_n)$ and $\xi_m = \xi(t_m, \vec{r}_m)$ and Bragg vectors $\vec{k}_n = \vec{k}(t_n, \vec{r}_n)$ and $\vec{k}_m = \vec{k}(t_m, \vec{r}_m)$. Using these definitions, we can inspect the covariance structure of the MLT wind fluctuations, by multiplying Equation 1 of the two meteors, and taking the expected value over multiple realizations of n and m:

$$\begin{aligned}\langle \omega_n \omega_m \rangle &= \langle \left(\vec{k}_n \cdot \vec{u}_n + \xi_n\right)\left(\vec{k}_m \cdot \vec{u}_m + \xi_m\right)\rangle \\ &= \langle \left(\vec{k}_n \cdot \vec{u}_n\right)\left(\vec{k}_m \cdot \vec{u}_m\right)\rangle + \langle \left(\vec{k}_n \cdot \vec{u}_n\right)\xi_m\rangle + \langle \left(\vec{k}_m \cdot \vec{u}_m\right)\xi_n\rangle + \langle \xi_n \xi_m\rangle.\end{aligned} \tag{4}$$

If the errors ξ_n and ξ_m are zero mean independent random variables ($m \neq n$), only the first term on the right-hand side is different than zero. We exclude cases where $n = m$ to avoid including correlated measurement errors $\langle \xi_n \xi_n \rangle \neq 0$. Expanding the resulting expression in terms of the vectors in LTz components, we have

$$\begin{aligned}\langle \omega_n \omega_m \rangle &= \langle (\vec{k}_n \cdot \vec{u}_n)(\vec{k}_m \cdot \vec{u}_m)\rangle \\ &= \langle (k_n^L u_n^L + k_n^T u_n^T + k_n^z w_n)(k_m^L u_m^L + k_m^T u_m^T + k_m^z w_m)\rangle \\ &= k_n^L k_m^L \langle u_n^L u_m^L\rangle + k_n^T k_m^T \langle u_n^T u_m^T\rangle + k_n^z k_m^z \langle w_n w_m\rangle \\ &+ \left(k_n^L k_m^T + k_n^T k_m^L\right)\langle u_n^L u_m^T\rangle + \left(k_n^L k_m^z + k_n^z k_m^L\right)\langle u_n^L w_m\rangle \\ &+ \left(k_n^T k_m^z + k_n^z k_m^T\right)\langle u_n^T w_m\rangle,\end{aligned} \tag{5}$$

where we have used the symmetry property $\langle u_n^i u_m^j \rangle = \langle u_n^j u_m^i \rangle$ (superscripts $i, j = L, T, z$ denote the different components). The velocity correlations $\langle u_n^i u_m^j \rangle$ can capture the structural properties of the mesoscale dynamics investigated in the present study. For simplicity of further analysis, let us define the velocity correlation tensor (R_{ij}) in the following form

$$R_{ij}\left(t_n, t_m, \vec{r}_n, \vec{r}_m\right) = \langle u_n^i u_m^j \rangle. \tag{6}$$

We can write $\omega_n \omega_m = \langle \omega_n \omega_m \rangle + \eta_{nm}$, with η_{nm} being a zero mean random variable with symmetric distribution. Then, Equation 5 has six unknowns, given by the correlation components defined in Equation 6, and can be rewritten as

$$\begin{aligned}\omega_n \omega_m = &k_n^L k_m^L R_{LL} + k_n^T k_m^T R_{TT} + k_n^z k_m^z R_{zz} \\ &+ \left(k_n^L k_m^T + k_n^T k_m^L\right) R_{LT} + \left(k_n^L k_m^z + k_n^z k_m^L\right) R_{Lz} + \left(k_n^T k_m^z + k_n^z k_m^T\right) R_{Tz} + \eta_{nm}.\end{aligned} \tag{7}$$

If we want to explore the solutions of Equation 7 in horizontal directions, the definition in Equation 6 simplifies to

$$R_{ij}\left(\tau, \vec{s}\right) = \langle u_n^i u_m^j \rangle. \tag{8}$$

Here, we consider homogeneity in horizontal L, T-directions and stationarity in time, so the correlation components do not depend on the positions and times, but on the differences of such quantities (Monin & Yaglom, 1971, p. 246). The vector $\vec{s} = \vec{r}_n - \vec{r}_m$ is the horizontal separation or spatial lag (illustrated in Figure 1a) and $\tau = t_n - t_m$ is the temporal lag. R_{LL} and R_{TT} are referred to as longitudinal and transverse components, respectively; and are expected to be much larger than R_{zz}, R_{Lz}, and R_{Tz} due to the buoyancy force effects that suppresses motions in the vertical direction. We do not test this theoretical assumption, although recent numerical simulations confirm that both horizontal components of mesoscale velocity are two orders of magnitude larger than the vertical component (u, $v \sim 20$ m s^{-1}, $w \sim 20$ cm s^{-1}; Avsarkisov et al., 2022). Also, our measurements suggest that R_{LL} and R_{TT} are larger than the horizontal cross-component R_{LT} when the winds are isotropic in the horizontal direction.

Under these considerations, a solution of Equation 7 is found by forming the following linear system

$$\begin{pmatrix} \vdots \\ \omega_n\omega_m \\ \vdots \end{pmatrix} = \begin{pmatrix} & \vdots & \\ k_n^L k_m^L & k_n^T k_m^T & k_n^z k_m^z & \left(k_n^L k_m^T + k_n^T k_m^L\right) & \left(k_n^L k_m^z + k_n^z k_m^L\right) & \left(k_n^T k_m^z + k_n^z k_m^T\right) \\ & \vdots & \end{pmatrix} \begin{pmatrix} R_{LL} \\ R_{TT} \\ R_{zz} \\ R_{LT} \\ R_{Lz} \\ R_{Tz} \end{pmatrix} + \begin{pmatrix} \vdots \\ \eta_{nm} \\ \vdots \end{pmatrix}, \quad (9)$$

which is then treated as a minimization problem in the sense of linear least squares to solve for R_{ij}. The way that the pairs of meteor echo Doppler shifts are combined to solve the system determines whether the method retrieves temporal or spatial correlations and what temporal and spatial lags are measured. This is a key step to obtain reliable values of correlations, as it is explained in Section 2.2.

To quantify the uncertainties in estimating the correlations, two procedures are followed in this work. The first one consists of estimating the typical least-squares uncertainties using the design matrix (assuming independent measurements), weighted by a factor that reduces the uneven hourly meteor counts effects during the day (Vierinen et al., 2019, Section 2.2). This is applied to the data from the Spread-spectrum Interferometric Meteor Observing Network (SIMONe) 2018 campaign (described in Section 3). The second procedure is applied to the longer data set, and consists of using sample statistics concepts to calculate reliable dispersion values, assuming that the correlations for every day and lag value are independent in a probabilistic sense.

2.2. Meteor-Pair Selection Procedure

In practice, to calculate horizontal spatial correlations $R_{ij}(\vec{s})$, the system in Equation 9 is solved for discrete values of $\vec{s}$, in a range whose upper limit is given by the geometry of the meteor radar network. The meteors are grouped in pairs to form the lagged products $\omega_n\omega_m$ that build the linear system and are the input to calculate the correlations for $\vec{s}$ values. Vierinen et al. (2019) proposed two solutions for WCFI's meteor pairing. In the first approach, the correlations are two dimensional, that is, distributed in east-west (s_x) and north-south (s_y) separations, with $\vec{s} = (s_x, s_y)$. This approach was implemented by Poblet et al. (2022), who described its properties in detail. The second approach is the one-dimensional approach, implemented in the original WCFI report (Vierinen et al., 2019), that retrieves correlations as functions of horizontal radial separations $|\vec{s}| = s_h = \sqrt{s_x^2 + s_y^2}$. The latter is followed in this work.

Since SMRs detect meteors in ~70–110 km altitude almost continuously in time, the first step to pairing meteor detections is to confine them to smaller altitude ranges, working with intervals of 2 km (Vierinen et al., 2019) or 6 km wide (Charuvil Asokan et al., 2022; Poblet et al., 2022), and daily or weekly spans, for example.

Then, from the selected detections, we proceed with one detection at the time as follows. We select a meteor n and tune the vertical and temporal conditions, finding every detection that is separated from it by not more than a temporal and vertical resolution ($\delta\tau$ and δz, respectively). Typical values of $\delta\tau$ can be 15 or 30 min, and 1 km for δz. After that, for each detection fulfilling the temporal and vertical requirements, only the ones that lie in the interval $s_h \pm \delta s_h/2$, for particular values of s_h, and fixed horizontal lag resolution δs_h, are chosen. The meteor pairs are formed by combining n with all other selected detections. The procedure is repeated, by selecting other detections to play the role of n. In the end, every pair has in common that their elements preserve the distance between each other under certain limits, given by $s_h \pm \delta s_h/2$. Finally, using non-repeated pairs, the system in Equation 9 is solved for the components of $R_{ij}(s_h)$.

The number of meteor pairs is a combination of the geographic distribution of the meteor detections and the size of the search area given by:

$$A = 2\pi s_h \delta s_h, \quad (10)$$

that depends only on s_h when the resolution δs_h is kept constant.

2.3. Fluctuating Wind Correlations

To study phenomena in different spatiotemporal scales, it is often convenient to separate the wind into a background or mean wind part $(\vec{U})$ part and a fluctuating part $(\vec{u}')$ using the Reynolds decomposition:

$$\vec{u} = \vec{U} + \vec{u}', \tag{11}$$

where $\langle \vec{u}' \rangle = 0$. The separation is highly dependent on the averaging procedure, and it is essential to identify and characterize high-frequency components of the wind, for instance, gravity waves (GWs) activity (Strelnikova et al., 2020). In terms of correlation functions, we perform the separation in the following manner. First, we solve Equation 1 for the background $\vec{U}$, using low temporal and spatial resolutions. Then, the values of $\vec{U}$ and ω are used to estimate high-pass-filtered Doppler-shift estimates ω', by calculating $\omega' = \omega - \vec{U} \cdot \vec{k}$. After that, ω' and $\vec{k}$ are used to estimate the correlation functions of the fluctuating wind R'_{ij}, with the method described in Section 2.1. For this work, the zonal and meridional components of $\vec{U}$ were calculated every 30 min and 1 km gates in altitude, using resolutions of 4 hr and 4 km. No horizontal gradients were included. These are rather restrictive values to resolve correlations of MLT mesoscale fluctuations, especially when we compare with the values used in previous works (e.g., Strelnikova et al., 2020). Yet, they work well in practice to diminish strong directionalities from the full-wind correlations (see Poblet et al., 2022, Figure 4). Following the notation in Equation 11, we use primes to denote the correlations of the fluctuating wind as well.

It is important to note that $\vec{U}$ still has an important effect in estimating the correlation functions. The temporal lag-resolution parameter $\delta\tau$, which indicates the maximum temporal separation between two meteors, will affect the correlation function. The smaller the horizontal scales being investigated, the smaller $\delta\tau$ has to be, or otherwise the mean wind will cause a significant decorrelation. This is because $\vec{U}$ transports smaller scale fluctuations. For example, if the mean horizontal wind velocity is $|\vec{U}| = 50$ m s^{-1}, and $\delta\tau = 1{,}000$ s, then an up to a 50 km difference in the location of a small scale turbulent eddy measured by two different meteors is possible.

3. Data Sets

The two data sets used in this study are the measurements from the 1-week SIMONe 2018 campaign (Charuvil Asokan et al., 2022; Vargas et al., 2021; Vierinen et al., 2019; Volz et al., 2021), and the 1-year measurements (March 2021–February 2022) collected from the Multistatic and Multifrequency Agile Radar for Investigations of the Atmosphere (MMARIA) network (Stober & Chau, 2015), hereinafter referred to as MMARIA-Germany 2021–2022. The measurements were taken over nearly the same geographical region in northern Germany so they provide both, short- and long-term insights into an atmospheric volume within a common region. The measurements consist of Bragg wave vectors, Doppler shifts, observation times, and the positions of specular meteor trails.

The SIMONe 2018 campaign was conducted for seven consecutive days between 2 November and 9 November. The radar network comprised two pulsed and one-coded-continuous-wave transmitters, and 14 receiving sites that detected about 1 million specular meteors with peaks in meteor counts at $\sim 87 - 96$ km altitude. SIMONe 2018 has been employed by several studies so far (i.e., Charuvil Asokan et al., 2022; Poblet et al., 2022; Vargas et al., 2021; Vierinen et al., 2019; Volz et al., 2021). These works present additional details about the systems, for example, the horizontal counts distribution (Poblet et al., 2022, Figure 1), the vertical counts distribution (Charuvil Asokan et al., 2022, Figure 1c), and location of the receiving sites (Charuvil Asokan et al., 2022, Table 1). This data set helps us to compare the method described in this work with the approach presented by Poblet et al. (2022), which uses exactly the same measurements.

The MMARIA-Germany 2021–2022 observations were obtained over Germany with the network of multistatic SMRs operated by the Leibniz Institute of Atmospheric Physics at the University of Rostock in Kühlungsborn, Germany; in collaboration with Leipzig University and the German Space Agency in Neustrelitz, both institutions located in Germany as well. During this period, the system consisted of three transmitters located in Kühlungsborn (54.15°N, 11.76°E), Collm (51.31°N, 13.00°E) and Juliusruh (54.63°N, 13.37°E). Kühlungsborn and Collm operated coded-CW and pulsed sequences, respectively. On the other hand, the Juliusurh system operated with pulsed sequences until July 2021, and since then with coded-CW sequences. The codes used in Juliusruh were different than the codes in Kühlungsborn, to facilitate the signal separation at the receiving stations.

On reception, Neustrelitz (53.33°N, 13.07°E) and Bornim (52.44°N, 13.02°E) sites consist of 10 receivers each, that are able to receive all three transmitter signals, while the other single-receiver sites receive only Kühlungsborn before July 2021, and Juliusruh-Kühlungsborn afterward. In summary, there have been two receiver stations with Multiple-Input Multiple Output (MIMO), five(four) receivers with Single-Input Multiple-Output (SIMO), and one(two) receiver(receivers) with Multiple-Input Multiple-Output (MISO) before(after) July 2021. These configurations make a total of 9(11) multistatic links before(after) July 2021. More single receivers are being continuously added to the network. Currently, the network has 17 multistatic links, that can be monitored on the website (MMARIA/SIMONe Germany Real-time Monitor Webpage, 2023). For details about MIMO, SIMO, and MISO techniques we refer the reader to Chau et al. (2019).

The standard deviation of the position error of specular meteor trails has been estimated by Chau et al. (2019) to be approximately 5 km in the horizontal direction and 1 km in the vertical direction. This estimate is derived by comparing the positions of meteors using two independent methods, angle of departure and angle of arrival interferometry solutions. Meteor trails with low elevation angles can be particularly affected by position errors so every meteor detected below 35° from the horizon was excluded from the MMARIA-Germany 2021–2022 database. The effect of position errors is important, as it limits the achievable lag resolution. The result is a database with more than 47,800 meteors per day on average, which allows us to cover horizontal separation distances for the correlation functions up to 400 km with good coverage (see Section 2.2).

Figure 2a presents a 2D histogram of the total number of specular meteor observations of MMARIA-Germany 2021–2022. It shows the number of detections within bins of 0.01° wide in latitude and longitude. The largest number of counts is concentrated between the ∼53–55.2° latitudinal range and the ∼10.5–15° longitudinal range. Similarly, Figure 2b presents an altitude histogram that shows a clean symmetric distribution of the meteor counts peaking at 90 km. Regarding the temporal evolution, Figures 2c and 2d show the daily number of detections for the year and its UT distribution, respectively. The counts show peaks in early May and mid-December, and a yearly evolution with more values during summer than during late winter, on average. This was also reported, for example, by Singer et al. (2004) and Haldoupis et al. (2007). The meteors are clearly more frequent in the morning and less frequent in the afternoon.

Figure 3 shows the number of meteor pairs in the two-dimensional (2D) and one-dimensional (1D) pairing procedures, introduced in Section 2.2, for the SIMONe 2018 campaign data. To be consistent, the same parameters were used for each plot, that is, we selected a 6 km wide altitude range between 87 and 93 km (i.e., centered at the peak of meteor counts), with $\delta\tau = 30$ min and $\delta z = 1$ km. Panel (a) shows the number of meteor pairs when the 2D procedure is followed. For this case, the pairs are distributed in s_x and s_y directions, with resolutions of $\delta s_x = 25$ km and $\delta s_y = 25$ km, respectively (Poblet et al., 2022, Section 3.3). Panel (b) presents the number of pairs as a function of horizontal separation s_h, when the one-dimensional approach with $\delta s_h = 25$ km is followed (blue line), using SIMONe 2018. In addition, we added the number of pairs in the 2D approach in the direction given by $s_x = 0$ and $s_y > 0$. The comparison between both curves demonstrates that, except for the shortest lags, the 2D method uses more than an order of magnitude fewer meteor pairs to resolve correlations in any direction than in the 1D approach. When s_h takes larger values, the searching area A starts to grow, and the number of meteors for pairing in the 1D approach increases rapidly, departing from the number of meteors that the 2D constant searching-area, given by $\delta s_x \delta s_y$, can detect. Note also that the peak in the pairs count for the 1D method is not located in the shortest separations region but around $s_h = 160$ km.

Figure 3c shows contours of the number of meteor pairs for each day of MMARIA-Germany 2021–2022 within the altitude range considered, as a function of s_h, using the 1D approach. They reach maximum values of about 10^7 pairs in April 2021. The yearly evolution of pairs number is a combination of two factors. These are, the instrumental factor, since the permanent meteor radar network was modified and expanded several times during the time period considered here, and the geophysical factor, since the largest number of specular meteor trails for this region is known to occur during summer and the lowest during late winter, as mentioned before.

4. Results

4.1. Validation

Figures 4a and 4b present a comparison between the new method (direct method), presented in this paper and the method described by Poblet et al. (2022) using the SIMONe 2018 data set (indirect method). Panel (a) shows R'_{LL}

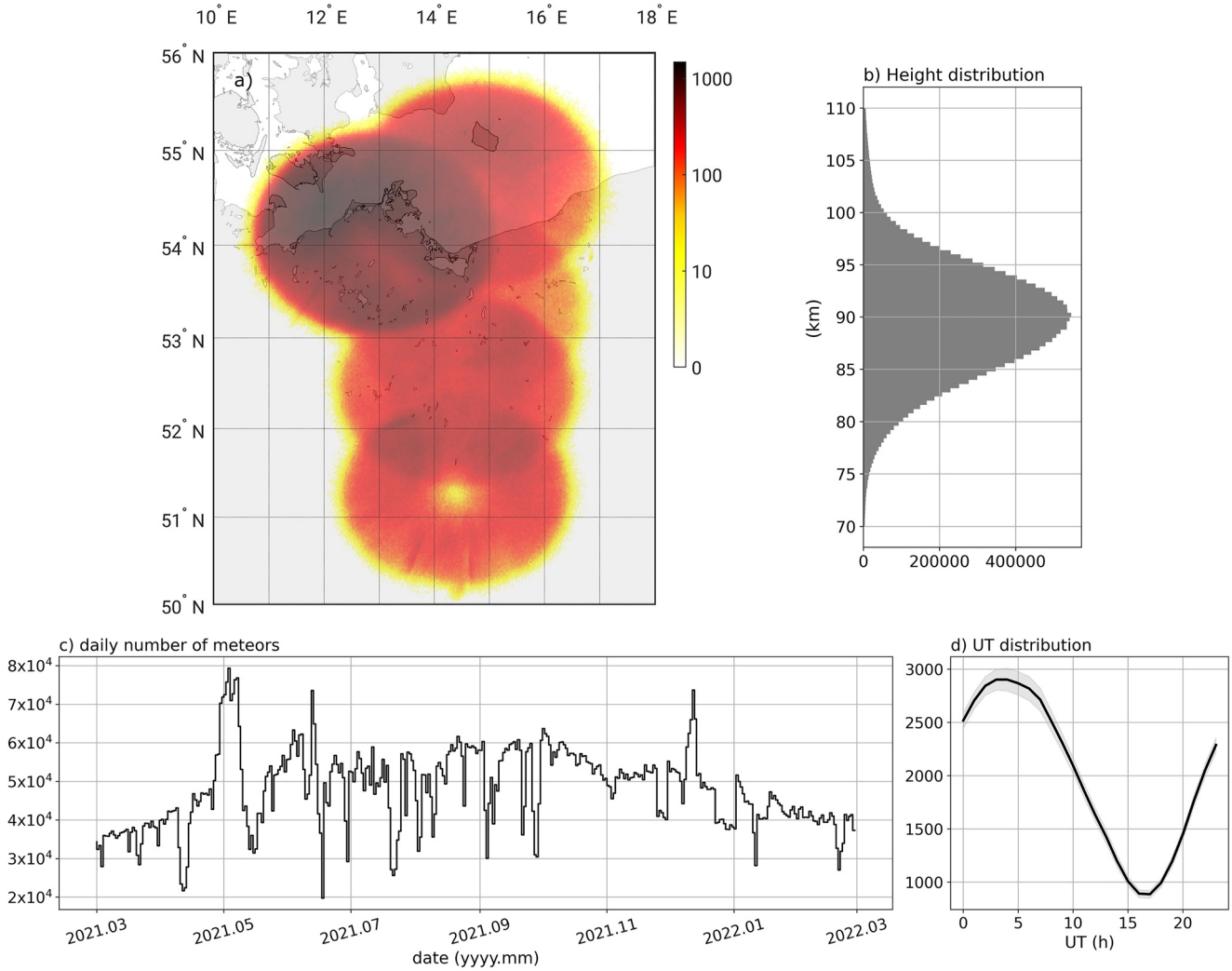

Figure 2. MMARIA-Germany 2021–2022 meteor detections. (a) 2D histogram for the total number of specular meteor observations detected between March 2021 and February 2022 in the MMARIA Germany network. The color bar values show the number of detections within bins of 0.01° wide in latitude and longitude. (b) Histogram showing the total number of meteor detections as a function of altitude (detections within the 87–93 km range were used in this work). (c) Daily number of meteors. (d) Number of meteor detections as a function of UT hour. The black curve shows the average number of meteors for the particular UT hour, using the complete year of measurements. The shaded gray area marks the 99% confidence interval. Only filtered measurements were used for every plot.

and panel (b) shows R'_{TT}, both as a function of horizontal spatial lag s_h. The mean-wind removal was carried out directly over the measured Doppler shift values, using the method outlined in Section 2.3. The estimates shown in black color were taken directly from Poblet et al. (2022), and represent the correlations calculated with the indirect method. This method first estimates 2D horizontal correlation functions of u and v distributed in s_x and s_y, and then analytically converts them to one dimensional R'_{LL} and R'_{TT} components. The olive-color curves in Figures 4a and 4b are the correlations estimated with the direct method described in this work. Since the number of meteor pairs in the 1D pairing procedure approach is much larger, we can use a higher lag resolution of $\delta s_h = 12.5$ km. The remaining parameters stay equal to the ones used for the plots shown in Figure 3.

The correlations estimated with both techniques show good agreement. They capture the general trend, that is, a progressive decorrelation as the separations increase. However, the direct method has two important benefits: the errors are significantly smaller and the correlations of shorter horizontal lags can be resolved.

The reason why shorter lags are not measured with the indirect approach is the following. When converting the 2D u and v correlation components to R'_{LL} and R'_{TT} components, we must assume that every meteor to be paired, detected within a 2D resolution of $\delta\vec{s} = (\delta s_x, \delta s_y)$, has the same ϕ value. This condition does not hold when

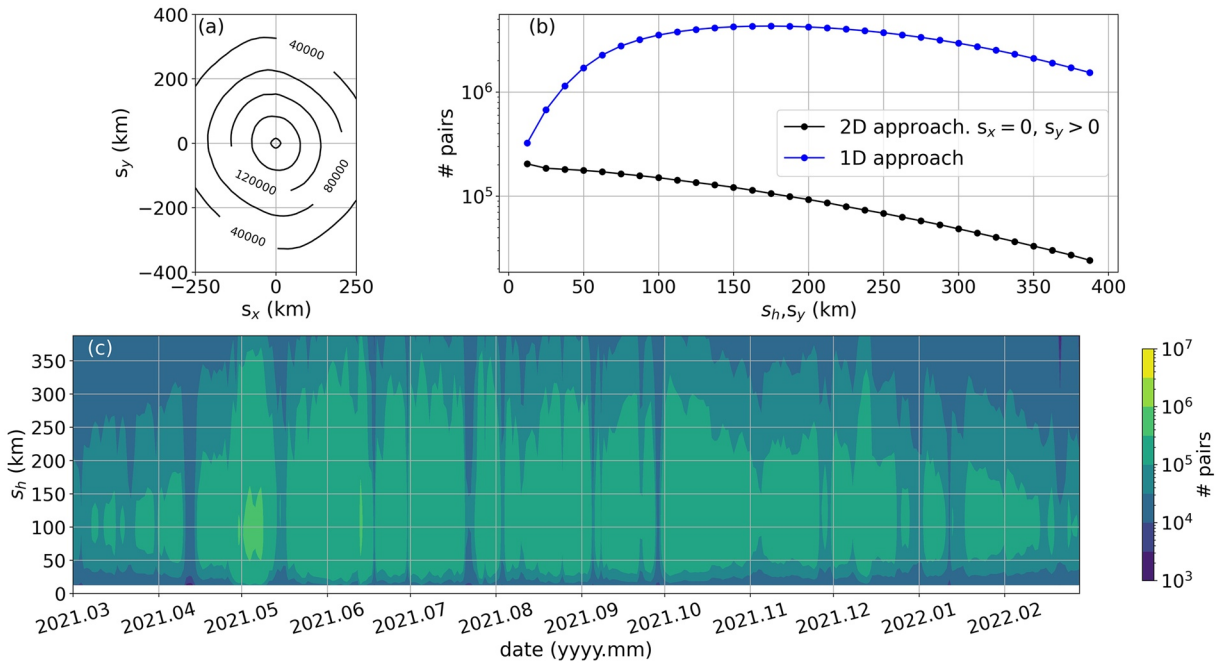

Figure 3. Results of the two-dimensional and one-dimensional meteor pair selection procedures. (a) Number of meteor pairs as a function of two-dimensional spatial separations $\vec{s} = (s_x, s_y)$ for the SIMONe 2018 campaign data. (b) Number of meteor pairs as a function of one-dimensional separations s_h for SIMONe 2018 (blue line). The black line marks the number of meteor pairs using the 2D approach of panel (a) for $s_x = 0$ and $s_y > 0$. (c) Daily number of meteor pairs using the one-dimensional approach for MMARIA-Germany 2021–2022. The parameters for all plots are $\delta\tau = 30$ min, $\delta z = 1$ km, $\delta s_h = \delta s_x = \delta s_y = 25$ km.

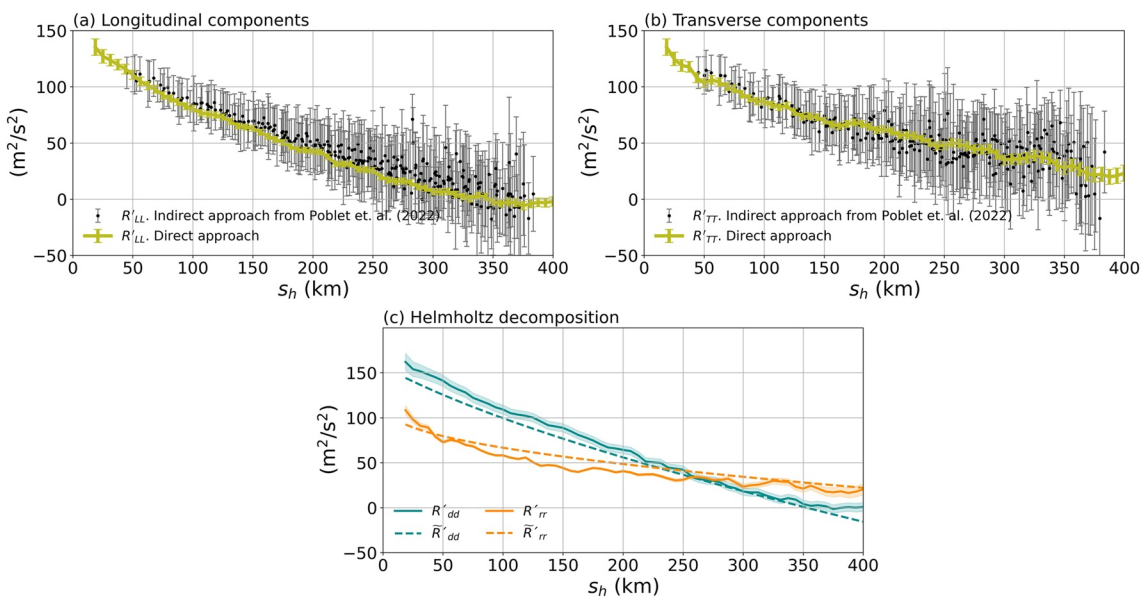

Figure 4. (a) Comparison between the two methods to estimate the longitudinal correlation functions of the fluctuating wind (R'_{LL}). The black dots are the correlations of the longitudinal component estimated with the indirect method reported in Poblet et al. (2022). The olive-color curve represents the longitudinal correlations estimated with the direct method reported in this work. (b) Similar to (a), for the transverse correlation component (R'_{TT}). (c) Helmholtz decomposition of the wind velocity correlations. The cyan and orange solid lines represent the spatial correlation of the divergent (R'_{dd}) and rotational (R'_{rr}) parts, respectively. The decomposition can also be determined analytically using longitudinal and transverse component fits and is shown as dashed curves. The reader is referred to Section 4.3 for details.

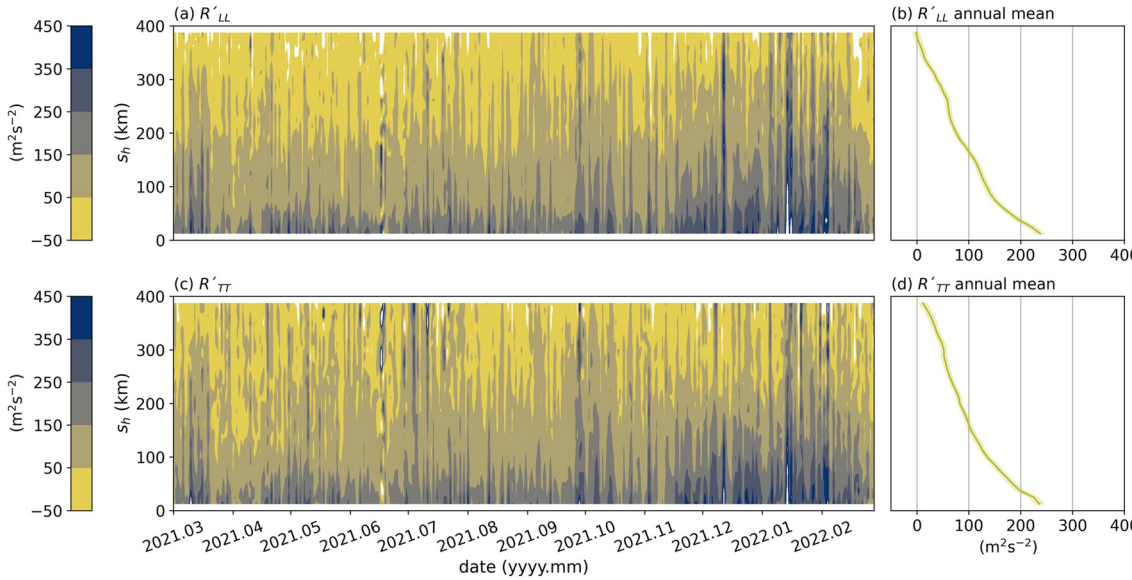

Figure 5. Correlation functions for 1 year of observations using MMARIA-Germany 2021–2022. (a) Contour plot showing daily, one dimensional R'_{LL} values as function of the horizontal lag s_h for the complete year of observations. (b) Annual means of R'_{LL} for each s_h value. The shadowed areas mark the 90% confidence interval. (c) Same as (a) but for the R'_{TT} component. (d) Annual mean values of R'_{TT}.

$|\delta\vec{s}| \sim |\vec{s}|$, so the shortest lags region must be excluded from the analysis (Poblet et al., 2022, Section 3). This requirement does not exist in the new method.

4.2. Annual Variability of R'_{LL} and R'_{TT}

The method was applied to the longer MMARIA-Germany 2021–2022 data set to study the annual variability of horizontal correlation functions. As for several time periods the daily meteor count was significantly smaller in this data set than in the SIMONe 2018 data set, the correlation functions will only be estimated with reasonably low errors using the new technique.

Figures 5a and 5c present longitudinal $\left(R'_{LL}\right)$ and transverse $\left(R'_{TT}\right)$ correlation functions, calculated for each day as a function of s_h. The parameters employed to calculate the correlations are the same as those used for meteor pairing in Figure 3c. The predominant feature is the decreasing of both components as s_h increases, as expected for turbulent fluctuations. This demonstrates that even using daily estimations, the method performs well. However, some days present clearly unphysical results where $R'_{ii}(s_h) > R'_{ii}(0)$, violating the so-called Schwarz inequality for fluctuating fields (Batchelor, 1953, p. 24), for example, in mid June and July. Based on visual inspection of mean wind estimates, these outliers occur at time periods where there are false detections of specular meteor trail echoes due to radio interference. These outliers were removed for the calculation of the annual means curves (introduced below) and for every other averaged curve in this work.

Interestingly, both components show increased levels of correlation around winter times, between mid November and mid March, which means that there is a seasonal behavior in the fluctuating wind correlations, on horizontal scales up to about 400 km. Figures 5b and 5d show the annual means of $R'_{LL}(s_h)$ and $R'_{TT}(s_h)$, respectively; in which the shadowed areas mark 90% confidence intervals on averaging over multiple days. From these plots, it is clear that both components reach similar zero-lag values of about 240 $m^2\ s^{-2}$ and they decrease smoothly toward larger separations, where R'_{TT} is slightly larger than R'_{LL}. This means that longitudinal and transverse fluctuations are balanced on small horizontal scales, but for larger scales, the kinetic energy is larger for transverse fluctuations than for longitudinal fluctuations. A similar result is observed for SIMONe 2018 in Figures 4a and 4b. This could be due to vorticity effects from larger scales eddies.

To explore the interplay between R'_{LL} and R'_{TT} in more detail, we generated monthly averages for both components. They are shown in Figure 6 along with the 90% confidence intervals (shadowed areas) calculated

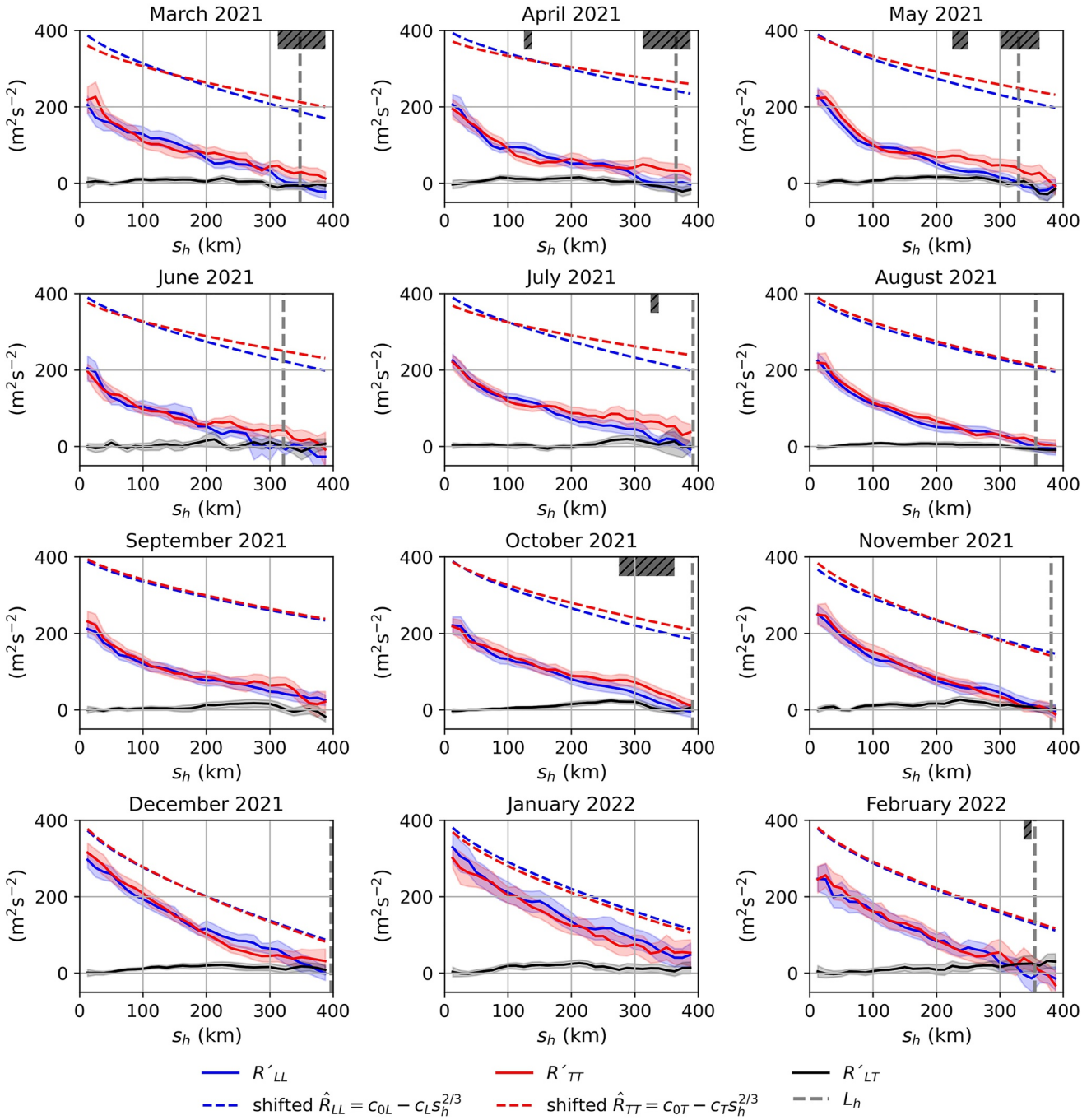

Figure 6. Monthly means of the longitudinal (blue line) and transverse (red line) correlation components of the fluctuating wind (R'_{LL} and R'_{TT}, respectively) combining the daily curves of Figure 5. The shadowed areas mark the 90% confidence intervals. The best fits, shown with dashed lines, are shifted in the vertical direction to avoid cluttering the figure. The vertical gray lines mark the characteristic horizontal length scale of stratified turbulence L_h. Hatched boxes on top of the plots mark the s_h regions where R'_{LL} is statistically different than R'_{TT}.

with the t-student distribution. The blue(red) solid line corresponds to the monthly means of $R'_{LL}(R'_{TT})$. The cross-correlation component R'_{LT} is also shown as black solid lines.

The consistent characteristic of each panel is that the monthly means of R'_{LL} and R'_{TT} decrease almost identically for growing separations. Following the trends of these components to small s_h values, they appear to converge to the same zero-lag value, which is different for each month. As expected, the larger values of correlations near the winter months identified in Figure 5 are also evident, especially in December and January. There are,

however, clear differences between both components for large enough lags, that occur in May, July, and October. On these months, R'_{TT} is larger than R'_{LL} for $s_h \gtrsim 200$ km, decorrelating at longer separations. The s_h ranges for which $R'_{LL} \neq R'_{TT}$ with a statistical significance level of 90% is shown by hatched boxes for each plot of the figure. Note that, even though the monthly means of R'_{LT} remain close to zero for every month and s_h value, it is slightly larger for months and lags with non-negligible $R'_{TT} - R'_{LL}$ values, for example, in May, July, and October.

A physical notion of how the fluctuations decorrelate in space can be gained by fitting the monthly means using the functions

$$\hat{R}_{LL} = c_{0L} - c_L s_h^{2/3}, \tag{12}$$

$$\hat{R}_{TT} = c_{0T} - c_T s_h^{2/3}. \tag{13}$$

The form of these functions is obtained by considering the following two arguments. First, we have to use the relation between second-order structure functions (D_{ii}, with $i = L, T$) and spatial autocorrelation functions. The former are defined by $D_{ii}(\vec{s}) = \langle \left[u^i(\vec{r}_n) - u^i(\vec{r}_m)\right]^2 \rangle$, that can be expanded to obtain

$$D_{ii}(\vec{s}) = \langle u^i(\vec{r}_n) u^i(\vec{r}_n) \rangle + \langle u^i(\vec{r}_m) u^i(\vec{r}_m) \rangle - 2\langle u^i(\vec{r}_n) u^i(\vec{r}_m) \rangle. \tag{14}$$

The first two terms on the right-hand side are correlations at zero lag $(\vec{s} = 0)$ for velocity products at different points (see Equation 8). Under homogeneity, they are $R_{ii}(0) = \langle u^i(\vec{r}_n) u^i(\vec{r}_n) \rangle = \langle u^i(\vec{r}_m) u^i(\vec{r}_m) \rangle$. Regarding the third term on the right-hand side, this is $-2R_{ii}(\vec{s})$. With these considerations, Equation 14 can be rearranged as

$$R_{ii}(\vec{s}) = R_{ii}(0) - \frac{1}{2} D_{ii}(\vec{s}). \tag{15}$$

The second argument for the choice of the functions in Equations 12 and 13 comes from Kolmogorov's isotropic turbulence. The first and second similarity hypotheses in this theory predict that in the inertial subrange the components of D_{ii} as a function of s_h will follow (Kolmogorov, 1941).

$$D_{LL}(s_h) = C_k (\epsilon_0 s_h)^{2/3}, \tag{16}$$

$$D_{TT}(s_h) = \frac{4}{3} C_k (\epsilon_0 s_h)^{2/3}. \tag{17}$$

The constant C_k is a universal constant, which has a value of $C_k \simeq 2.0$ (Davidson, 2013; Ellsaesser, 1969) and ϵ_0 is the turbulent energy transfer rate. Substituting Equation 16 in Equation 15, it is straightforward to obtain the functional dependence given by Equation 12, in which the parameters contain the information of the zero-lag correlation and the constants involved in Equation 16. Exactly the same procedure can be followed for the transverse component using Equations 13, 15, and 17. Note that, from Equations 16 and 17, $D_{TT} = (4/3)D_{LL}$.

The local horizontal homogeneity and isotropy of the wind field assumed above are well-known features also for ST theory (e.g., Riley & Lindborg, 2008, and references therein). In this study, we follow Avsarkisov et al. (2022) and postulate that this theory can also explain the mesoscale dynamics in the MLT region.

The monthly fits $\hat{R}_{LL}$ and $\hat{R}_{TT}$ are shown in Figure 6 as dashed blue and red lines, but shifted by a constant along the ordinate axis in such a way that the highest zero-lag value between both components is at 410 m^2 s^{-2}. This shift is performed for clarity purposes, so one can clearly distinguish between the characteristics of the measured and fitted curves. The estimated parameter values are presented in Table 1. It can be observed that the fits follow the monthly means behavior of the measured correlation functions (R'_{LL} and R'_{TT}) fairly well. In several months, the agreement with a 2/3-power law of separation distance is remarkable; for instance, in March, December, and January. Yet, other months show slight departures from the theory, especially for short separations, for example, April, May, and June.

We can directly use the parameters c_{0L} and c_L from Equation 12, to approximate the largest horizontal scale up to which the wind fluctuation dynamics is explained by ST, that is, the integral length scale:

$$L_h = \frac{\sigma_u^3}{\epsilon_0}. \tag{18}$$

Table 1
Coefficient Values of $\hat{R}_{LL} = c_{0L} - c_L s_h^{2/3}$, $\hat{R}_{TT} = c_{0T} - c_T s_h^{2/3}$, $\hat{R}_{dd} = c_{0d} - c_d s_h^{2/3}$ *and* $\hat{R}_{rr} = c_{0r} - c_r s_h^{2/3}$

mm.yyyy	c_{0L}	c_L	c_{0T}	c_T	c_L/c_T	c_{0d}	c_d	c_{0r}	c_r
03.2021	221.59 ± 3.78	4.45 ± 0.11	215.30 ± 6.48	3.93 ± 0.18	1.13 ± 0.06	238.35 ± 5.95	4.70 ± 0.17	198.36 ± 5.89	3.67 ± 0.17
04.2021	192.87 ± 6.37	3.88 ± 0.18	171.14 ± 9.08	3.03 ± 0.26	1.28 ± 0.12	196.30 ± 6.91	3.84 ± 0.20	169.94 ± 9.86	3.16 ± 0.28
05.2021	216.20 ± 6.34	4.61 ± 0.18	213.82 ± 9.10	3.96 ± 0.26	1.16 ± 0.09	262.64 ± 7.64	5.51 ± 0.22	168.57 ± 8.50	3.11 ± 0.25
06.2021	203.52 ± 5.57	4.37 ± 0.16	184.37 ± 5.19	3.40 ± 0.15	1.29 ± 0.07	225.00 ± 5.31	4.67 ± 0.15	161.94 ± 6.82	3.05 ± 0.20
07.2021	225.80 ± 3.87	4.27 ± 0.11	205.25 ± 5.88	3.18 ± 0.16	1.34 ± 0.08	250.37 ± 3.66	4.60 ± 0.11	180.14 ± 7.32	2.82 ± 0.21
08.2021	214.36 ± 5.80	4.35 ± 0.16	223.34 ± 5.28	4.42 ± 0.15	0.98 ± 0.05	236.10 ± 7.10	4.85 ± 0.20	203.73 ± 4.22	4.01 ± 0.12
09.2021	209.76 ± 4.22	3.61 ± 0.12	221.38 ± 6.88	3.79 ± 0.20	0.95 ± 0.06	228.96 ± 6.05	4.04 ± 0.17	203.05 ± 5.92	3.39 ± 0.17
10.2021	237.69 ± 3.20	4.49 ± 0.09	228.94 ± 3.82	3.83 ± 0.10	1.17 ± 0.04	263.90 ± 2.88	4.93 ± 0.08	201.10 ± 4.49	3.33 ± 0.13
11.2021	257.20 ± 4.40	4.96 ± 0.12	272.05 ± 2.90	5.37 ± 0.08	0.92 ± 0.03	269.73 ± 5.79	5.31 ± 0.17	260.04 ± 2.23	5.05 ± 0.06
12.2021	326.53 ± 3.38	6.05 ± 0.10	340.35 ± 7.84	6.45 ± 0.22	0.94 ± 0.04	331.03 ± 6.08	6.23 ± 0.18	338.60 ± 6.54	6.39 ± 0.19
01.2022	345.70 ± 4.12	5.85 ± 0.12	324.38 ± 4.95	5.56 ± 0.14	1.05 ± 0.03	309.22 ± 3.88	5.08 ± 0.12	364.34 ± 5.55	6.47 ± 0.16
02.2022	279.16 ± 3.80	5.54 ± 0.11	286.34 ± 5.15	5.60 ± 0.15	0.99 ± 0.03	296.44 ± 4.65	5.91 ± 0.13	267.29 ± 4.86	5.16 ± 0.14

Note. The values of c_L/c_T illustrate the relative contributions of divergent and vortical motions (see text for details). Zero-lag coefficients are in units of $m^2\ s^{-2}$, and first-order coefficients in units of $10^{-2}\ m^{4/3}\ s^{-2}$.

Here, σ_u is the root mean square (RMS) velocity of the fluctuations in the horizontal direction, that can be approximated by $\sigma_u = \sqrt{c_{0L}}$. In the above formula, the transfer rate ϵ_0 is estimated using Equations 15 and 16, which results in $\epsilon_0 = c_L^{3/2}$, assuming that the Kolmogorov constant is $C_k = 2$. This length scale is expected to be in the order of 100 km in the lower thermosphere (Avsarkisov, 2020; Avsarkisov et al., 2022), but as both σ_u and ϵ_0 vary, L_h also varies. Gray vertical dashed lines have been added to the panels of Figure 6 centered in the abscissa value given by L_h. Interestingly, L_h is large enough to cover the majority of the s_h range, and in some cases L_h is larger than its maximum value (e.g., September, December, and January). The mean value is $L_h = 380$ km.

4.3. Helmholtz Decomposition

Lindborg (2014) discusses a Helmholtz decomposition that can be used to represent the horizontal wind velocity as a sum of purely rotational $(\vec{u}^r)$ and purely divergent $(\vec{u}^d)$ components:

$$\vec{u} = \vec{u}^r + \vec{u}^d = -\nabla \times \left(\vec{e}_z \Psi\right) + \nabla_h \Phi. \tag{19}$$

In this equation, Ψ is the stream function, $\vec{e}_z$ is the vertical unit vector, Φ is the velocity potential, and ∇_h is the horizontal gradient operator. As discussed by Lindborg (2014), it is possible to convert longitudinal and transverse correlation functions to divergent and rotational correlation functions using the following expressions:

$$R_{rr}(s_h) = R_{TT}(s_h) - \int_{s_h}^{\infty} \frac{R_{TT}(\eta) - R_{LL}(\eta)}{\eta} \mathrm{d}\eta, \tag{20}$$

$$R_{dd}(s_h) = R_{LL}(s_h) + \int_{s_h}^{\infty} \frac{R_{TT}(\eta) - R_{LL}(\eta)}{\eta} \mathrm{d}\eta. \tag{21}$$

The rotational and divergent correlation functions are defined as $R_{rr}(s_h) = \langle \vec{u}^r(\vec{r}_n) \cdot \vec{u}^r(\vec{r}_m) \rangle$ and $R_{dd}(s_h) = \langle \vec{u}^d(\vec{r}_n) \cdot \vec{u}^d(\vec{r}_m) \rangle$, with $s_h = |\vec{r}_n - \vec{r}_m|$ being the distance between two position vectors $\vec{r}_n$ and $\vec{r}_m$ that are displaced from one another purely in the horizontal direction.

Equations 20 and 21 are useful from a numerical point of view because integrating over a function has a tendency to average out noise, which means that this transformation should be relatively robust to uncorrelated measurement errors.

The divergent and rotational correlations of the fluctuating wind R'_{dd} and R'_{rr} were calculated numerically using Simpson's rule over the monthly means of R'_{LL} and R'_{TT}. These are shown in Figure 7, in which the cyan line

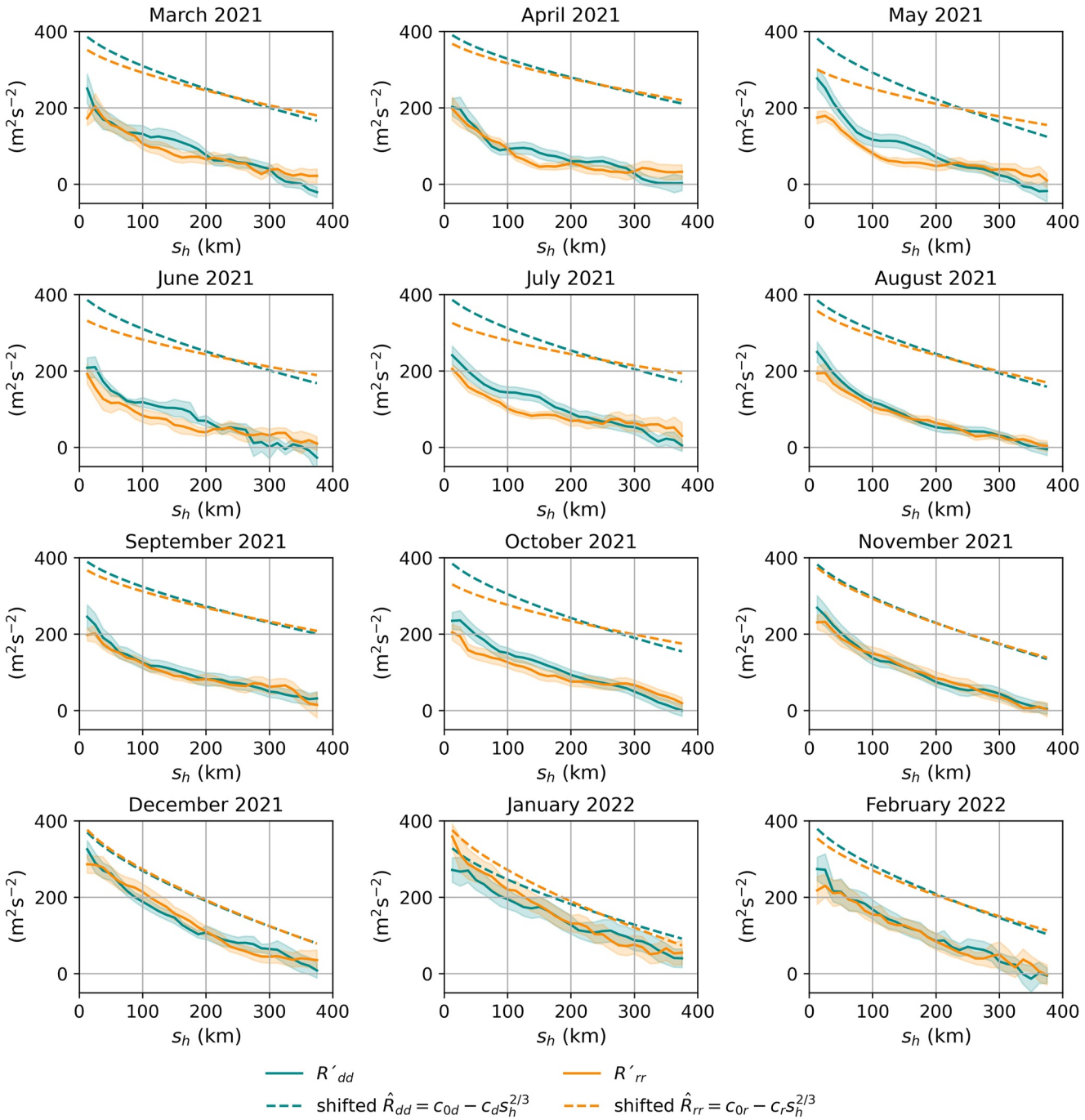

Figure 7. Monthly, divergent (cyan line) and rotational (orange line) correlation components. The shadowed areas mark the 90% confidence intervals. The best fits, shown with dashed lines, are shifted in the vertical direction to avoid cluttering the figure.

corresponds to R'_{dd} and the orange line to R'_{rr}. From a general inspection of every panel, it is evident that the two components are nearly equal in magnitude most of the time. Similarly to R'_{LL} and R'_{TT}, the rotational and divergent correlations present elevated correlation values during the winter months and the best fits capture the main features of the measured correlations fairly well. The overall physical interpretation is that kinetic energy is, to first order, balanced between divergent and vortical modes and that during the winter months, there is more kinetic energy in the fluctuations than in the summer months.

Subtle differences between R'_{dd} and R'_{rr} occur in the months with the largest differences between transverse and longitudinal correlations $\left(R'_{TT} - R'_{LL}\right)$. This is because the integrands in Equations 20 and 21 are significant for these cases. This effect is more prominent in summer, in May, June, and July, but it is also evident in October. Note that in these months, while the differences between the longitudinal and transverse components occur for the largest horizontal lags, they are observed in the short lags region for R'_{dd} and R'_{rr}. During these months, R'_{dd} dominates over R'_{rr} up to around 250 km, where there is a crossing point from which $R'_{rr} > R'_{dd}$ for larger separations. This separation value is consistent with the transition scale size found by Roberts and Larsen (2014), using horizontal structure functions of expanding chemical tracers in the mesosphere. Slight deviations between rotational and divergent correlations can also be seen in the months of March, December, and January, which show repeated crossing points at different s_h values. However, these deviations for the most part are not statistically significant.

Figure 4c shows the Helmholtz decomposition for the SIMONe 2018 data set. Since $R'_{TT} - R'_{LL}$ was clear for this 1-week campaign, there is a crossing point between both components that appears around $s_h = 275$ km, similar to what several months in Figure 7 show.

The differences between R'_{dd} and R'_{rr} for the SIMONe 2018 data set are much larger than they are for the monthly averages shown in Figure 7, presumably due to the shorter time window over which the correlations are estimated, indicating that while on a monthly time scale, the energy appears to be equipartitioned between vortical and divergent modes, on shorter times scales this is not necessarily the case. Validating this hypothesis is a topic for future work.

By fitting R'_{LL} and R'_{TT} using Equations 12 and 13, we can analytically estimate the Helmholtz decomposition, solving Equations 20 and 21. These analytical solutions for rotational $\left(\tilde{R}_{rr}\right)$ and divergent $\left(\tilde{R}_{dd}\right)$ components are shown as dashed lines in Figure 4c. Although there is a very good agreement between the numerical and analytical determinations, the numerical estimates capture irregularities and small changes in the trends that are lost when a simplified theoretical model is used to represent R'_{LL} and R'_{TT}.

It is interesting to compare R'_{dd} and R'_{rr} with the correlation functions of vertical vorticity $\zeta_z\left(\vec{r}\right) = \left[\nabla \times \vec{u}'\left(\vec{r}\right)\right] \cdot \vec{e}_z$ and horizontal divergence for fluctuating winds, defined as $Q_{zz} = \langle \zeta_z\left(\vec{r}\right)\zeta_z\left(\vec{r}+\vec{s}\right)\rangle$ and $P = \langle \left(\nabla_h \cdot \vec{u}'_h\left(\vec{r}\right)\right)\left(\nabla_h \cdot \vec{u}'_h\left(\vec{r}+\vec{s}\right)\right)\rangle$, respectively (Lindborg, 2007). In P, the divergence operator is applied over the horizontal wind components, indicated with subindex h. Both analyses pursue the same goal, which is to disentangle the vortical and divergent modes, but they differ in practice since Q_{zz} and P incorporate an extra second-order derivative. They are related as follows: $Q_{zz} = -\nabla^2 R'_{rr}$ and $P = -\nabla^2 R'_{dd}$ (Li & Lindborg, 2018; Lindborg, 2014). The numerical calculation of Q_{zz} and P from R'_{LL} and R'_{TT} is then more unstable, as measurement errors tend to be amplified by the ∇^2 operator. Poblet et al. (2022) have calculated Q_{zz} and P using the parameters resulting from fitting R'_{LL} and R'_{TT} and using the following equations (see Lindborg (2007) or Poblet et al. (2022) for details):

$$Q_{zz}(s_h) = \frac{1}{s_h}\frac{\mathrm{d}R'_{LL}(s_h)}{\mathrm{d}s_h} - \frac{1}{s_h^2}\frac{\mathrm{d}}{\mathrm{d}s_h}\left(s_h^2\frac{\mathrm{d}R'_{TT}(s_h)}{\mathrm{d}s_h}\right), \tag{22}$$

$$P(s_h) = \frac{1}{s_h}\frac{\mathrm{d}R'_{TT}(s_h)}{\mathrm{d}s_h} - \frac{1}{s_h^2}\frac{\mathrm{d}}{\mathrm{d}s_h}\left(s_h^2\frac{\mathrm{d}R'_{LL}(s_h)}{\mathrm{d}s_h}\right). \tag{23}$$

They found that P was more than five times larger than Q_{zz}. If we repeat this calculation with R'_{LL} and R'_{TT} using the new direct method presented in this paper, we obtain that P is around three times larger than Q_{zz}. Both estimations are in the same order of magnitude, but as expected, they do not fully agree. The differences must be attributed to the inherent errors of the fitting procedure.

Equations 22 and 23 can also be used to quantify the relative importance of divergent and rotational parts, by deriving relations for the cases of the fluctuating field behaving purely like a GW field ($Q_{zz} = 0$) or a 2D vorticity field ($P = 0$). Setting $Q_{zz} = 0$ in Equation 22 and integrating, we obtain

$$R_{LL} = \frac{\mathrm{d}}{\mathrm{d}s_h}(s_h\, R_{TT}). \tag{24}$$

Considering the representation of R_{LL} and R_{TT} given by Equations 12 and 13 and replacing them in Equation 24, it is obtained that the ratio $c_L/c_T = 5/3 \simeq 1.6$. Similarly, using Equation 23 for a 2D vorticity field, the ratio between the coefficients is $c_L/c_T = 3/5 \simeq 0.6$. This means that for the limits of a full GW field or a full 2D vorticity field,

the quotients c_L/c_T should be close to 5/3 or 3/5, respectively. The observed ratios c_L/c_T for the monthly fits shown in Figure 6 are given in Table 1. The values are between the limits for each month, and in most cases near the value $\frac{1}{2}(5/3 + 3/5) \simeq 1.1$, that is, the mean of values 5/3 and 3/5. This indicates again, that both the divergent and vortical parts contribute to explaining the mesoscale dynamics of fluctuating wind correlations on a monthly timescale.

5. Discussion

It has been demonstrated that using the LTz decomposition of the $\vec{k}$ vectors as an input to the WCFI method leads to a more efficient estimation of the horizontal correlation functions $R'_{LL}(s_h)$ and $R'_{TT}(s_h)$ compared to the indirect method. An important factor in this improvement is the significant increase in the number of meteor pairs obtained when detections are grouped over every horizontal direction. The disadvantage of this procedure is that we lose the correlation information for particular horizontal directions in the 2D horizontal plane.

The new approach to estimate $R'_{LL}(s_h)$ and $R'_{TT}(s_h)$ was applied to the longer MMARIA-Germany 2021–2022 data set to infer nominal characteristics when they are estimated over a common geographical region over 1 year. The method was implemented in the region with the maximum number of meteor detections, that is, at 87–93 km of altitude. The correlations in this region exhibited increased values during the winter months, particularly in December and January, indicating the prevalence of wind fluctuations during this time of the year. This maximum has also been found by the composite analysis of mean wind residuals performed by Conte et al. (2018) in the same region as studied in this work. The authors calculated a proxy of the residual-wind's kinetic energy for each day of the year and considered increased GWs activity as the source of the enhanced winter values.

It is also possible that part of the winter fluctuations correspond to secondary GWs (Vadas et al., 2018). This reasoning is justified by results of general circulation model simulations by Avsarkisov et al. (2022), who found for winter conditions at ~60°N (i.e., close to the latitudes explored in this work), turbulent RMS velocities with two peaks centered at around 60 and 105 km altitude (see Avsarkisov et al., 2022, Figure 10). Since this parameter is proportional to the turbulent energy dissipation rate, the authors speculated that the lower peak could be associated with the breaking of primary waves, that then excite upward propagating secondary GWs, which dissipate near the height of the second peak. Vertical wavelengths and periods of secondary GWs have been observed to be larger than 6 km and 6 hr (Vadas et al., 2018; Zhao et al., 2017); so the major part of them should be removed when we subtract the influence of large-scale phenomena in our analysis. Yet, a small portion can remain and contribute to the increased correlation values that we observed during the winter months.

The analysis of the monthly divergent and rotational parts, as well as of the longitudinal and transverse parts, reveals a clear equipartition between both correlation components for a wide range of separations. This implies that neither the 3D isotropic relation $D'_{TT} = (4/3)D'_{LL}$ of Kolmogorov (1941) nor the scaling law for a 2D isotropic flow $D'_{TT} = (5/3)D'_{LL}$ (Lindborg, 1999) are valid. Such relations have rarely been reported for structure functions measured in the UTLS, in which the transverse component is increasingly larger than the longitudinal component as the separation increases. According to Frehlich and Sharman (2010), the transverse component for $s_h > 50$ km is more affected by planetary waves. For $s_h \simeq 300$–800 km, Lindborg (1999) found that the differences between structure-function components can be explained by considering the relation between longitudinal and transverse structure functions components for a 2D turbulent flow (Lindborg, 1999, Equation 53). In our case, these differences between R'_{TT} and R'_{LL} are probably lost when removing background wind effects.

However, for spring and summer months, R'_{TT} and R'_{LL} present small but statistically significant discrepancies. During these months, the transverse component decorrelates at longer lags, which is reflected as a clear prevalence of R'_{dd} over R'_{rr} for the shortest horizontal lags. The larger magnitude of the divergent part during these months highlights the dominant role of the GW dynamics since all the energy of GWs is contained in the divergent part (Davidson, 2013). In these months, R'_{dd} exhibits a plateau for $s_h \simeq 75$–150 km. Such unusual behavior can be a sign of the existence of a local source of secondary GWs, which are usually present in the mesopause region during the summer months, but its presence in the spring months requires additional considerations.

The good agreement of the observations with a $s_h^{2/3}$ power law indicates the turbulent nature of the fluctuations, with a downscale cascade of energy. This behavior, encountered almost every month, allowed us to estimate a coarse limit up to which ST theory may explain our observations, given by the length scale L_h. The results showed

that L_h is rather large and contains the majority of the s_h range, indicating that ST might provide a physical framework to explain the horizontal correlation functions of the fluctuating wind.

6. Concluding Remarks and Implications

We have presented a robust technique to estimate horizontal, longitudinal and transverse correlation functions of MLT wind fluctuations. Second-order estimates have played an important role in the last few decades, to acquire more insight into the turbulent nature of the atmospheric flow (Lilly, 1983; Lindborg, 2007). Based on lower atmospheric research applications, our technique can be applied to study several topics in the MLT. For instance, it can be used to estimate energy transfer rates, which has been treated as a complementary step to estimate L_h in the paper, but this would warrant a more extensive future study on its own. This would signify an additional method to the already existing in situ (Lübken, 1997) or MF radar based (Hocking & Mu, 1997) techniques. Another interesting avenue of research is the analysis of the wavenumber spectrum of wind fluctuations based on the horizontal correlation functions, which can delve into more information on how the energy is distributed across different scales. This topic has been intensively discussed in the UTLS (e.g., Callies et al., 2016), but so far only been accessible for the MLT region using polar mesospheric summer and winter echoes traced by powerful VHF radars (e.g., Ecklund & Balsley, 1981; Rapp & Lübken, 2004; Sato et al., 2017).

The application of the method to a single meteor-radar network is particularly suitable for the study of the mesoscales because the correlations for $\lesssim$500 km separations can be investigated. However, some of the already existing networks could be combined to study larger-scale correlations. These are the cases, for instance, of SIMONe Germany (Chau et al., 2019) and SIMONe Norway (Huyghebaert et al., 2022), or the SIMONe Peru (Chau et al., 2021) and SIMONe Argentina (Conte et al., 2021).

Data Availability Statement

The specular meteor radar data products used to produce the figures presented in this article can be found in HDF5 format in Poblet (2023).

Acknowledgments
We thank Nico Pfeffer and Matthias Clahsen for their vital help in maintaining the MMARIA Germany meteor radar network. We also thank Dr. Hans Pécseli and Dr. Fabio Feraco for the interesting discussions and for reading the manuscript. The work of J.F.C. was partially supported by the Bundesministerium für Bildung und Forschung via project WASCLIM-IAP, part of the ROMIC-II program. Also, the wok of V.A. is financed by the Leibniz SAW project FORMOSA (Grant K227/2019). H. C. A. is supported by DFG under SPP 1788 Dynamic Earth CH1482/2, and by the French Ministry of Foreign and European Affairs for the Eiffel excellence scholarship (File N945179K). Open Access funding enabled and organized by Projekt DEAL.

References

Avsarkisov, V. (2020). On the buoyancy subrange in stratified turbulence. *Atmosphere*, *11*(6), 659. https://doi.org/10.3390/atmos11060659

Avsarkisov, V., Becker, E., & Renkwitz, T. (2022). Turbulent parameters in the middle atmosphere: Theoretical estimates deduced from a gravity wave–resolving general circulation model. *Journal of the Atmospheric Sciences*, *79*(4), 933–952. https://doi.org/10.1175/JAS-D-21-0005.1

Batchelor, G. K. (1953). *The theory of homogeneous turbulence*. Cambridge University Press.

Buell, C. E. (1960). The structure of two-point wind correlations in the atmosphere. *Journal of Geophysical Research*, *65*(10), 3353–3366. https://doi.org/10.1029/jz065i010p03353

Callies, J., Bühler, O., & Ferrari, R. (2016). The dynamics of mesoscale winds in the upper troposphere and lower stratosphere. *Journal of the Atmospheric Sciences*, *73*(12), 4853–4872. https://doi.org/10.1175/JAS-D-16-0108.1

Charuvil Asokan, H., Chau, J. L., Marino, R., Vierinen, J., Vargas, F., Urco, J. M., et al. (2022). Frequency spectra of horizontal winds in the mesosphere and lower thermosphere region from multistatic specular meteor radar observations during the SIMONe 2018 campaign. *Earth Planets and Space*, *74*(1), 74–69. https://doi.org/10.1186/s40623-022-01620-7

Chau, J. L., Urco, J. M., Vierinen, J., Harding, B. J., Clahsen, M., Pfeffer, N., et al. (2021). Multistatic specular meteor radar network in Peru: System description and initial results. *Earth and Space Science*, *8*(1), e2020EA001293. https://doi.org/10.1029/2020ea001293

Chau, J. L., Urco, J. M., Vierinen, J. P., Volz, R. A., Clahsen, M., Pfeffer, N., & Trautner, J. (2019). Novel specular meteor radar systems using coherent MIMO techniques to study the mesosphere and lower thermosphere. *Atmospheric Measurement Techniques*, *12*(4), 2113–2127. https://doi.org/10.5194/amt-12-2113-2019

Cho, J. Y. N., & Lindborg, E. (2001). Horizontal velocity structure functions in the upper troposphere and lower stratosphere: 1. Observations. *Journal of Geophysical Research*, *106*(D10), 10223–10232. https://doi.org/10.1029/2000jd900814

Conte, J. F., Chau, J. L., Laskar, F. I., Stober, G., Schmidt, H., & Brown, P. (2018). Semidiurnal solar tide differences between fall and spring transition times in the northern hemisphere. *Annales Geophysicae*, *36*(4), 999–1008. https://doi.org/10.5194/angeo-36-999-2018

Conte, J. F., Chau, J. L., Urco, J. M., Latteck, R., Vierinen, J., & Salvador, J. O. (2021). First studies of mesosphere and lower thermosphere dynamics using a multistatic specular meteor radar network over southern Patagonia. *Earth and Space Science*, *8*(2), e2020EA001356. https://doi.org/10.1029/2020ea001356

Davidson, P. A. (2004). *Turbulence. An introduction for scientists and engineers*. Oxford University Press.

Davidson, P. A. (2013). *Turbulence in rotating, stratified and electrically conducting fluids*. Cambridge University Press.

Ecklund, W., & Balsley, B. (1981). Long-term observations of the arctic mesosphere with the MST radar at poker flat, Alaska. *Journal of Geophysical Research*, *86*(A9), 7775–7780. https://doi.org/10.1029/ja086ia09p07775

Ellsaesser, H. W. (1969). A climatology of epsilon (atmospheric dissipation). *Monthly Weather Review*, *97*(6), 415–423. https://doi.org/10.1175/1520-0493(1969)097⟨0415:ACOED⟩2.3.CO;2

Frehlich, R., & Sharman, R. (2010). Climatology of velocity and temperature turbulence statistics determined from rawinsonde and ACARS/AMDAR data. *Journal of Applied Meteorology and Climatology*, *49*(6), 1149–1169. https://doi.org/10.1175/2010jamc2196.1

Gage, K. (1979). Evidence far a $k^{-5/3}$ law inertial range in mesoscale two-dimensional turbulence. *Journal of the Atmospheric Sciences*, *36*(10), 1950–1954. https://doi.org/10.1175/1520-0469(1979)036<1950:efalir>2.0.co;2

Haldoupis, C., Pancheva, D., Singer, W., Meek, C., & MacDougall, J. (2007). An explanation for the seasonal dependence of midlatitude sporadic *E* layers. *Journal of Geophysical Research*, *112*(A6), A06315. https://doi.org/10.1029/2007JA012322

Hamilton, K., Takahashi, Y. O., & Ohfuchi, W. (2008). Mesoscale spectrum of atmospheric motions investigated in a very fine resolution global general circulation model. *Journal of Geophysical Research*, *113*(D18). D18110. https://doi.org/10.1029/2008jd009785

Hocking, W., Fuller, B., & Vandepeer, B. (2001). Real-time determination of meteor-related parameters utilizing modern digital technology. *Journal of Atmospheric and Solar-Terrestrial Physics*, *63*(2–3), 155–169. https://doi.org/10.1016/s1364-6826(00)00138-3

Hocking, W., & Mu, P. (1997). Upper and middle tropospheric kinetic energy dissipation rates from measurements of C_n^2—Review of theories, *in situ* investigations, and experimental studies using the Buckland Park atmospheric radar in Australia. *Journal of Atmospheric and Solar-Terrestrial Physics*, *59*(14), 1779–1803. https://doi.org/10.1016/S1364-6826(97)00020-5

Holdsworth, D. A., Reid, I. M., & Cervera, M. A. (2004). Buckland Park all-sky interferometric meteor radar. *Radio Science*, *39*(5). https://doi.org/10.1029/2003rs003014

Huyghebaert, D., Clahsen, M., Chau, J. L., Renkwitz, T., Latteck, R., Johnsen, M. G., & Vierinen, J. (2022). Multiple E-region radar propagation modes measured by the VHF SIMONe Norway system during active ionospheric conditions. *Frontiers in Astronomy and Space Sciences*, *9*. https://doi.org/10.3389/fspas.2022.886037

King, G. P., Vogelzang, J., & Stoffelen, A. (2015a). Second-order structure function analysis of scatterometer winds over the tropical Pacific. *Journal of Geophysical Research: Oceans*, *120*(1), 362–383. https://doi.org/10.1002/2014jc009992

King, G. P., Vogelzang, J., & Stoffelen, A. (2015b). Upscale and downscale energy transfer over the tropical Pacific revealed by scatterometer winds. *Journal of Geophysical Research: Oceans*, *120*(1), 346–361. https://doi.org/10.1002/2014jc009993

Kolmogorov, A. N. (1941). The local structure of turbulence in incompressible viscous fluid for very large Reynolds numbers. *Doklady Akademii Nauk SSSR*, *30*, 301–305.

Li, Q., & Lindborg, E. (2018). Weakly or strongly nonlinear mesoscale dynamics close to the tropopause? *Journal of the Atmospheric Sciences*, *75*(4), 1215–1229. https://doi.org/10.1175/JAS-D-17-0063.1

Lilly, D. K. (1983). Stratified turbulence and the mesoscale variability of the atmosphere. *Journal of the Atmospheric Sciences*, *40*(3), 749–761. https://doi.org/10.1175/1520-0469(1983)040⟨0749:STATMV⟩2.0.CO;2

Lindborg, E. (1999). Can the atmospheric kinetic energy spectrum be explained by two-dimensional turbulence? *Journal of Fluid Mechanics*, *388*, 259–288. https://doi.org/10.1017/S0022112099004851

Lindborg, E. (2006). The energy cascade in a strongly stratified fluid. *Journal of Fluid Mechanics*, *550*, 207–242. https://doi.org/10.1017/s0022112005008128

Lindborg, E. (2007). Horizontal wavenumber spectra of vertical vorticity and horizontal divergence in the upper troposphere and lower stratosphere. *Journal of the Atmospheric Sciences*, *64*(3), 1017–1025. https://doi.org/10.1175/jas3864.1

Lindborg, E. (2014). A Helmholtz decomposition of structure functions and spectra calculated from aircraft data. *Journal of Fluid Mechanics*, *762*. R4. https://doi.org/10.1017/jfm.2014.685

Lübken, F.-J. (1997). Seasonal variation of turbulent energy dissipation rates at high latitudes as determined by in situ measurements of neutral density fluctuations. *Journal of Geophysical Research*, *102*(D12), 13441–13456. https://doi.org/10.1029/97JD00853

Marenco, A., Thouret, V., Nédélec, P., Smit, H., Helten, M., Kley, D., et al. (1998). Measurement of ozone and water vapor by airbus in-service aircraft: The MOZAIC airborne program, an overview. *Journal of Geophysical Research*, *103*(D19), 25631–25642. https://doi.org/10.1029/98jd00977

MMARIA/SIMONe Germany Real-time Monitor Webpage. (2023). Retrieved from http://maarsy.rocketrange.no/SIMONe/SIMONe_GER/index.html

Monin, A. S., & Yaglom, A. M. (1971). *Statistical fluid mechanics* (Vol. 1). The Massachussetts Institute of Technology Press.

Nastrom, G. D., Gage, K. S., & Jasperson, W. H. (1984). Kinetic energy spectrum of large-and mesoscale atmospheric processes. *Nature*, *310*(5972), 36–38. https://doi.org/10.1038/310036a0

Poblet, F. L. (2023). *Data files*. RADAR—Research Data Repository. https://dx.doi.org/10.22000/807

Poblet, F. L., Chau, J. L., Conte, J. F., Avsarkisov, V., Vierinen, J., & Asokan, H. C. (2022). Horizontal wavenumber spectra of vertical vorticity and horizontal divergence of mesoscale dynamics in the mesosphere and lower thermosphere using multistatic specular meteor radar observations. *Earth and Space Science*, *9*(9), e2021EA002201. https://doi.org/10.1029/2021EA002201

Rapp, M., & Lübken, F.-J. (2004). Polar mesosphere summer echoes (PMSE): Review of observations and current understanding. *Atmospheric Chemistry and Physics*, *4*(11/12), 2601–2633. https://doi.org/10.5194/acp-4-2601-2004

Richardson, L. F. (1922). Weather prediction by numerical process. *Quarterly Journal of the Royal Meteorological Society*, *48*(203), 282–284.

Riley, J. J., & Lindborg, E. (2008). Stratified turbulence: A possible interpretation of some geophysical turbulence measurements. *Journal of the Atmospheric Sciences*, *65*(7), 2416–2424. https://doi.org/10.1175/2007jas2455.1

Roberts, B., & Larsen, M. (2014). Structure function analysis of chemical tracer trails in the mesosphere-lower thermosphere region. *Journal of Geophysical Research: Atmospheres*, *119*(11), 6368–6375. https://doi.org/10.1002/2013jd020796

Rodriguez Imazio, P., Dörnbrack, A., Urzua, R. D., Rivaben, N., & Godoy, A. (2022). Clear air turbulence observed across a tropopause fold over the drake passage—A case study. *Journal of Geophysical Research: Atmospheres*, *127*(4), e2021JD035908. https://doi.org/10.1029/2021jd035908

Sato, K., Kohma, M., Tsutsumi, M., & Sato, T. (2017). Frequency spectra and vertical profiles of wind fluctuations in the summer Antarctic mesosphere revealed by MST radar observations. *Journal of Geophysical Research: Atmospheres*, *122*(1), 3–19. https://doi.org/10.1002/2016jd025834

Singer, W., von Zahn, U., & Weiß, J. (2004). Diurnal and annual variations of meteor rates at the arctic circle. *Atmospheric Chemistry and Physics*, *4*(5), 1355–1363. https://doi.org/10.5194/acp-4-1355-2004

Skamarock, W. C., Park, S.-H., Klemp, J. B., & Snyder, C. (2014). Atmospheric kinetic energy spectra from global high-resolution nonhydrostatic simulations. *Journal of the Atmospheric Sciences*, *71*(11), 4369–4381. https://doi.org/10.1175/jas-d-14-0114.1

Stober, G., & Chau, J. L. (2015). A multistatic and multifrequency novel approach for specular meteor radars to improve wind measurements in the MLT region. *Radio Science*, *50*(5), 431–442. https://doi.org/10.1002/2014rs005591

Strelnikova, I., Baumgarten, G., & Lübken, F.-J. (2020). Advanced hodograph-based analysis technique to derive gravity-wave parameters from lidar observations. *Atmospheric Measurement Techniques*, *13*(2), 479–499. https://doi.org/10.5194/amt-13-479-2020

Stull, R. B. (1988). *An introduction to boundary layer meteorology* (Vol. 13). Springer Science & Business Media.

Vadas, S. L., Zhao, J., Chu, X., & Becker, E. (2018). The excitation of secondary gravity waves from local body forces: Theory and observation. *Journal of Geophysical Research: Atmospheres*, *123*(17), 9296–9325. https://doi.org/10.1029/2017JD027970

Vargas, F., Chau, J. L., Asokan, H. C., & Gerding, M. (2021). Mesospheric gravity wave activity estimated via airglow imagery, multistatic meteor radar, and SABER data taken during the SIMONe–2018 campaign. *Atmospheric Chemistry and Physics*, *21*(17), 13631–13654. https://doi.org/10.5194/acp-21-13631-2021

Vierinen, J., Chau, J. L., Charuvil, H., Urco, J. M., Clahsen, M., Avsarkisov, V., et al. (2019). Observing mesospheric turbulence with specular meteor radars: A novel method for estimating second-order statistics of wind velocity. *Earth and Space Science*, *6*(7), 1171–1195. https://doi.org/10.1029/2019ea000570

Volz, R., Chau, J. L., Erickson, P. J., Vierinen, J. P., Urco, J. M., & Clahsen, M. (2021). Four-dimensional mesospheric and lower thermospheric wind fields using Gaussian process regression on multistatic specular meteor radar observations. *Atmospheric Measurement Techniques*, *14*, (11), 7199–7219. https://doi.org/10.5194/amt-2021-40

Zhao, J., Chu, X., Chen, C., Lu, X., Fong, W., Yu, Z., et al. (2017). Lidar observations of stratospheric gravity waves from 2011 to 2015 at McMurdo (77.84°S, 166.69°E), Antarctica: 1. Vertical wavelengths, periods, and frequency and vertical wave number spectra. *Journal of Geophysical Research: Atmospheres*, *122*(10), 5041–5062. https://doi.org/10.1002/2016JD026368